Adsorption 11: 455–477, 2005

Modeling of Adsorption in Finite Cylindrical Pores by Means of Density Functional Theory

E.A. USTINOV
On leave from Saint Petersburg State Technological Institute, Technical University, 26 Moskovsky, Prospect, 198013, Russia

D.D. DO*
Department of Chemical Engineering, University of Queensland, St. Lucia, Queensland 4072, Australia

Received February 7, 2005; Revised August 8, 2005; Accepted September 7, 2005

Abstract. Adsorption of argon at its boiling point in finite cylindrical pores is considered by means of the non-local density functional theory (NLDFT) with a reference to MCM-41 silica. The NLDFT was adjusted to amorphous solids, which allowed us to quantitatively describe argon adsorption isotherm on nonporous reference silica in the entire bulk pressure range. In contrast to the conventional NLDFT technique, application of the model to cylindrical pores does not show any layering before the phase transition in conformity with experimental data. The finite pore is modeled as a cylindrical cavity bounded from its mouth by an infinite flat surface perpendicular to the pore axis. The adsorption of argon in pores of 4 and 5 nm diameters is analyzed in canonical and grand canonical ensembles using a two-dimensional version of NLDFT, which accounts for the radial and longitudinal fluid density distributions. The simulation results did not show any unusual features associated with accounting for the outer surface and support the conclusions obtained from the classical analysis of capillary condensation and evaporation. That is, the spontaneous condensation occurs at the vapor-like spinodal point, which is the upper limit of mechanical stability of the liquid-like film wetting the pore wall, while the evaporation occurs via a mechanism of receding of the semispherical meniscus from the pore mouth and the complete evaporation of the core occurs at the equilibrium transition pressure. Visualization of the pore filling and empting in the form of contour lines is presented.

Keywords: density functional theory, adsorption, capillary condensation, MCM-41

1. Introduction

The capillary phenomenon in adsorption systems attracts attention of scientists for nearly a century. A new impulse to further investigation of adsorption mechanism is associated with the recent discovery of high-ordered mesoporous M41S materials (Kresge et al., 1992; Beck et al., 1992). One of the representatives of M41S family is the MCM-41 series of siliceous materials, which have a hexagonal arrangement of cylindrical pores. The pore size distribution (PSD) of MCM-41 silica is quite narrow, and its pore diameter is reliably determined independently by the XRD technique (Kruk et al., 1997a, 1997b; Dabadie et al., 1996). This is the reason why such materials can be used for experimental verification of different theories. Thus, it was shown that the Barrett–Joyner–Halenda (BJH) method (1951) of determination of PSD of adsorbents based on the Kelvin equation with a correction for the statistical film thickness (Gregg and Sing, 1982) substantially underestimates the pore size (Lastoskie et al., 1993). Some improvement of the Kelvin equation in an empirical manner suggested by Kruk, Jaroniec and Sayari (KJS) (1997c) has led to a quantitative description of the filling pressure versus diameter in the case of argon and nitrogen adsorption in MCM-41 series. This method

*To whom correspondence should be addressed.

has been successfully applied for the PSD analysis using the adsorption branch of the experimental isotherm. From the theoretical viewpoint the most rigorous classical theory is that of Broekhoff and de Boer (BdB) (1967a; 1967b; 1968a; 1968b; 1968c). This theory relies on the adsorption isotherm on the reference non-porous adsorbent having the same chemical structure of the surface as that of the pore walls. This is a rather critical assumption as it is generally expected that the surface of a porous material is not necessarily the same as that of the reference non-porous adsorbent. Nevertheless, it is often that this assumption is implicitly accepted in the analysis of porous materials. Results obtained with the BdB theory agree well with those obtained with more rigorous molecular approaches for the pore diameter larger than 7 nm (Neimark and Ravikovitch, 2001). Accounting for the dependence of surface tension on the meniscus curvature improved the BdB theory (Sonwane and Bhatia, 1998; Bhatia and Sonwane, 1998; Sonwane et al., 1998). However, the most adequate representation of adsorption mechanism in cylindrical pores may be achieved only with molecular approaches such as the non-local density functional theory (NLDFT) (Ravikovitch et al., 1997; Ravikovitch and Neimark, 2000, 2001; Neimark and Ravikovitch, 2001; Ravikovitch et al., 2001) and Monte Carlo simulation method (Neimark et al., 2000; Vishnyakov and Neimark, 2003). All classical and molecular theories in general support the classical explanation of the reason for the hysteresis advanced long ago (Everett, 1967). In accordance with this representation the capillary condensation occurs at the pressure (so called the vapor-like spinodal point) at which the metastable adsorbed film wetting the pore walls loses its mechanical stability, immediately followed a spontaneous filling of the pore volume. The evaporation occurs via a mechanism of receding of the semispherical menisci from the open ends of the cylindrical pore, and the evaporation of the inner core is completed at a pressure corresponding to the equilibrium transition. Nevertheless, the pattern of relationships in the adsorption mechanism even in the simplest case of cylindrical geometry is not completely understood. Moreover, the experimental observation in many cases unambiguously contradicts to theoretical predictions. For example, it was found from experimental data on nitrogen adsorption and desorption in MCM-41 silica at 77 K that the adsorption and desorption isotherms are reversible for pores of the diameter up to about 4 nm (Kruk et al., 1997a; Franke et al., 1993; Branton et al., 1993), above which a hysteresis loop occurs. This pore diameter of 4 nm is called the critical hysteresis pore diameter. Results from the DFT simulation give a value of 2 nm (Ravikovitch et al., 1997), which is far below that observed experimentally. This discrepancy was explained by accounting for the surface wall roughness, which causes the so called single-pore blocking effect (Inoue et al., 1998; Kruk et al., 2000). However, the estimation of the pore wall roughness of 0.1 nm given by Inoue et al. (1998) to provide the reversibility observed experimentally seems to be underestimated due to some thermodynamic incorrectness in the analysis of the desorption branch of the isotherm. Another way to overcome this difficulty was explored by Maddox et al. (1997) who introduced a two-dimensional periodic function for the solid–fluid potential in cylindrical pores to account for the energetic heterogeneity of the silica pore walls. This allows them to extend the reversible part of the condensation/evaporation pressure–diameter dependence up to the size of 2.8–3.2 nm.

Another problem is the lower limit of the hysteresis (Gregg and Sing, 1982; Kruk et al., 1997c; Ravikovitch and Neimark, 2001; Thommes et al., 2002; Kruk and Jaroniec, 2000; Kruk and Jaroniec, 2001). In the case of nitrogen adsorption at 77 K and argon adsorption at 87 K the hysteresis is not observed at relative pressures below 0.42 and 0.38, respectively. Besides, the steepness of desorption branch increases in the proximity of the lower limit of the hysteresis, which is not associated with the narrow pore size distribution (Kruk et al., 1997c; Kruk and Jaroniec, 2000). It seems to indicate that the evaporation occurs at the same pressure for pores of different diameters around of 4 nm (in the case of nitrogen) as if the stretched liquid were broken at a definite negative pressure. This argument is in line with the tensile strength hypotheses (Kadlec and Dubinin, 1969; Burgess et al., 1970; Selvam et al., 2001). However, so far this hypothesis has not been justified with the molecular approaches.

One more problem is that which branch of the isotherm is the equilibrium branch. The classical vision of the hysteresis phenomenon associates the evaporation with the equilibrium transition point. However, some authors relying on experimental data found (or implicitly assumed) that the adsorption branch is closer to the true equilibrium (Branton et al., 1993; Kruk et al., 1997c; Kruk and Jaroniec, 2002; Morishige and Ito, 2002; Morishige and Nakamura, 2004). For example, Morishige et al. (2002; 2004) investigated the dependence of the chemical potential at the condensation

and evaporation pressures on temperature for different species and pore diameters. This dependence is proved to be the straight line for the capillary condensation pressure in all range of temperature, while the dependence for the capillary evaporation pressure exhibits a kink at the hysteresis critical temperature. It suggests that below the hysteresis critical temperature it is the capillary condensation that occurs at thermodynamic equilibrium, rather than the evaporation. Some support of this conclusion was recently obtained by comparison of the experimental capillary condensation pressure–diameter dependence for nitrogen and argon adsorption at their respective boiling points and the curve for equilibrium transition predicted by the NLDFT (Ustinov and Do, 2004b; Ustinov et al., 2005b, 2005c). It was shown that for a definite value of the surface area of the reference non-porous silica these curves completely coincide, while the experimental evaporation–diameter curve cannot be described by the calculated equilibrium transition curve at all, no matter what value of the surface area of the reference silica is chosen.

All aforementioned experimentally observed features of adsorption systems have not been properly explained in the framework of the one-dimensional model of infinitely long cylindrical pore. This suggests that some light may be shed on this problem by analysis of filling and evaporation of the cylindrical pore from the pore mouth. Monte Carlo simulations provided recently for finite silica-like cylindrical pores seem to support such an expectation (Gelb, 2002). It was found that accounting for open pore mouths substantially reduces the width of hysteresis loop, with the pore end nucleating the capillary condensation. On the other hand, molecular simulations in a very long simulation cell of 108 collision diameters did not show any multi-domain structure near to the pressure of capillary condensation. It means an extremely low probability of spontaneous formation of liquid-like bridges, which would nucleate the condensation below the vapor-like spinodal point. Molecular dynamic calculations of adsorption hysteresis in narrow cylindrical pores with open ends in canonical ensemble (Heffelfinger et al., 1988), has confirmed the classical representation that the pore empting occurs via receding hemispherical menisci from the pore ends at the equilibrium transition pressure that is significantly higher than the pressure (liquid-like spinodal pressure), at which the appearance of bubbles could be observed in infinitely long pores. The latter was claimed to be an artifact of periodic boundary conditions. Analogous result was obtained with canonical Monte Carlo simulation for finite cylindrical pores by Papadopoulou et al. (1992). Non-local density functional theory was used for analysis of argon adsorption and desorption in finite cylindrical pores (Ustinov and Do, 2004a). In this work the pore wall was assumed smooth like graphite surface, which is suitable for modeling of adsorption in adsorbents like carbon nanotubes. Application of the two-dimensional Tarazona's version of NLDFT (accounting for the radial and axial density distribution) has led to solidification of argon at 87.3 K, which is above the triple point. It is still not clear, whether the solidification is not an artifact coming from the mean-field assumption used in the DFT. Nevertheless, it could be induced only by the strong radial layering of the fluid due to the smooth pore wall surface, which provokes the axial density oscillation resulting in the ordered (hexagonal) solid-like structure with the density markedly larger than that for the liquid argon (Ustinov and Do, 2004a). It suggests that in order to prevent the solidification the smooth pore wall surface should be replaced by the amorphous surface, which would allow us to model adsorption in such adsorbents as MCM-41 and SBA-15 silica. As far as we are aware of, there are no attempts to consider the mechanism of adsorption and desorption in open-ended cylindrical pore by means of 2D NLDFT. Besides there are no works in the literature, which consider the role of adsorption on the outer surface bounded the cylindrical pores from their end. Limited attempts along this line were made (Heffelfinger, 1988; Papadopoulou et al., 1992; Gelb, 2002; Ustinov and Do, 2004a), in which the pore mouth is modeled as a single tube, one section of which exerts an adsorption potential and the other is just a hard wall. Such a model is simple, but not realistic. At the same time the role of the external surface is not obvious and it is worthwhile to check, whether the formation of liquid film on the external surface could induce the nucleation of capillary condensation or delay the pore empting. In any case it seems to be likely if the external surface has larger adsorption potential than the internal cylindrical surface due to, for example, additional functional groups like silanols in the case of silica surface. Such problems have led us to the following aims in the present paper. The first aim is to build an approximate model of application the conventional non-local density functional theory to adsorption on disordered solids like silica. Second, we intend to consider the mechanism of condensation/evaporation in the finite open-ended cylindrical pore by means of the two-dimensional version of NLDFT (i.e. accounting

for the axial and radial fluid density distributions) in canonical and grand canonical ensembles accounting for the adsorption on the external surface adjoining to the pore entrance. The canonical NLDFT allows us to visualize the formation of hemispherical meniscus separating the liquid-like and the vapor-like sections of the adsorbed phase and trace its movement during capillary condensation and evaporation, which could provide a deeper insight to the real conditions at which the experimental adsorption is taken place.

2. Model

2.1. *Basic Assumptions of NLDFT and its Application for Confined Fluids*

In this paper we rely on the Tarazona's smoothed density approximation (Tarazona, 1985; Evans et al., 1986; Tarazona et al., 1987). In the case of open pore (grand canonical ensemble) the equilibrium fluid density distribution in a confined pore volume must correspond to the minimum of the following grand thermodynamic potential

$$\Omega = \int \rho(r)[f(r) - \mu]\, dr \tag{1}$$

Here ρ is the local density of the adsorbed fluid; f is the molecular Helmholtz free energy of the adsorbed phase; μ is the chemical potential, which is specified for each equilibrium point. The average number of molecules N in the pore volume V is

$$N = \int \rho(r)\, dr \tag{2}$$

The amount adsorbed is proportional to N, and the average fluid density adsorbed in the pore is N/V. In the case of close system (canonical ensemble) the number of molecule N in the pore is specified. The density distribution corresponds to the minimum of the Helmholtz free energy

$$F = \int \rho(r) f(r)\, dr \tag{3}$$

It should be noted that for small systems accommodating a few molecules the Helmholtz free energy may be different in canonical and grand canonical ensembles (Gonzalez et al., 1997; White and Gonzalez, 2002). However, in the present paper we deal with mesopores, rather than micropores. The simulation cell of about $1500\,\sigma_{ff}{}^3$, which we use in the NLDFT analysis, could accommodate about one thousand molecules. It means that the difference in the Helmholtz free energy defined in canonical and grand canonical ensembles is negligibly small.

The chemical potential μ corresponding to a given number of molecules N is given by

$$\mu = \left(\frac{\partial F}{\partial N}\right)_{T,V} \tag{4}$$

The Helmholtz free energy is represented as a sum of four terms as follows:

$$f(r) = k_B T[\ln(\Lambda^3 \rho(r)) - 1] + f_{\text{ex}}[\bar{\rho}(r)] + u^{\text{int}}(r) + u^{\text{ext}}(r) \tag{5}$$

In the right hand side (RHS) the terms are the ideal part, the excess part, the attractive potential of the intermolecular interactions, and the external potential exerted by the solid, respectively. Here Λ is the thermal de Broglie wavelength and k_B is Boltzmann's constant. The excess Helmholtz free energy, $f_{\text{ex}}(\bar{\rho})$, accounts for repulsive forces and is defined by the Carnahan–Starling (CS) equation (Carnahan and Starling, 1969) for the equivalent hard sphere fluid:

$$f_{\text{ex}}(\bar{\rho}) = k_B T \frac{4\bar{\eta} - 3\bar{\eta}^2}{(1-\bar{\eta})^2}, \quad \bar{\eta} = \frac{\pi}{6} d_{\text{HS}}^3 \bar{\rho} \tag{6}$$

Here d_{HS} is the equivalent hard sphere diameter; $\bar{\rho}$ is the smoothed density defined by the Tarazona prescription (Tarazona, 1985). The smoothed density $\bar{\rho}$ is the following weighting average

$$\bar{\rho}(\mathbf{r}) = \int \rho(\mathbf{r}')\omega(|\mathbf{r} - \mathbf{r}'|; \bar{\rho}(\mathbf{r}'))\, d\mathbf{r}' \tag{7}$$

The weight function $\omega(|\mathbf{r} - \mathbf{r}'|; \bar{\rho}(\mathbf{r}'))$ could be approximated with reasonable accuracy by the following quadratic dependence (Tarazona, 1985).

$$\bar{\rho}(\mathbf{r}) = \bar{\rho}_0(\mathbf{r}) + \bar{\rho}_1(\mathbf{r})\bar{\rho}(\mathbf{r}) + \bar{\rho}_2(\mathbf{r})(\bar{\rho}(\mathbf{r}))^2 \tag{8}$$

with

$$\bar{\rho}_i(\mathbf{r}) = \int \rho(\mathbf{r}')\omega_i(|\mathbf{r} - \mathbf{r}'|)d\mathbf{r}', \quad i = 0, 1, 2 \tag{9}$$

The weight functions $\omega_0(r)$, $\omega_1(r)$, and $\omega_2(r)$ are defined in the region $0 < r < 2\sigma_{ff}$ (Tarazona et al., 1987).

In the framework of the mean field approximation the attractive part of the Helmholtz free energy (the

potential of interaction of a fluid molecule with the surrounding fluid molecules) is given by:

$$u^{\text{int}}(\mathbf{r}) = \frac{1}{2}\int_{\text{Fluid}} \rho(\mathbf{r}')\phi_{ff}(|\mathbf{r}-\mathbf{r}'|)\,d\mathbf{r}' \qquad (10)$$

where the pair-wise attractive potential is defined in the form of the Weeks, Chandler and Andersen (WCA) equation (Weeks et al., 1971):

$$\phi_{ff}(r) = \begin{cases} -\varepsilon_{ff}, & r < r_m \\ 4\varepsilon_{ff}[(\sigma_{ff}/r)^{12} - (\sigma_{ff}/r)^6], & r_m < r < r_c \\ 0, & r > r_c \end{cases} \qquad (11)$$

Here r and r_c is the distance between the molecules and the cutoff distance, respectively; ε_{ff} is the potential well depth; σ_{ff} is the fluid – fluid collision diameter; $r_m = 2^{1/6}\,\sigma_{ff}$ is the distance at which the potential is minimum.

The external potential inside a pore is usually determined by integration of the 12-6 LJ pair-wise potential over the solid volume.

2.2. *A Method of Application of the NLDFT to Amorphous Solids*

Up to date the non-local density functional theory has been mostly applied to model the equilibrium adsorption only on crystalline surfaces like graphitized carbon black. The feature of such a model is that centers of the surface atoms of the solid are located in the two-dimensional space, which is either plane (graphitized carbon black, slit pore wall) or a closed surface of a simple geometry (cylindrical or spherical pore). The consequence of such a representation is that the locus of minimum of the potential exerted by the solid is also a surface, resulting in the formation of the 2D molecular layer of the adsorbed fluid. Being a source of the secondary potential field the first molecular layer induces the formation of the second molecular layer with an increase in the bulk pressure, and so forth. Molecular layering is an inherent feature of a smooth surface. Therefore using such a surface to model adsorption in amorphous solids like siliceous adsorbents by using either conventional DFT or Monte Carlo simulation always gives rise to a large deviation between theoretical and experimental adsorption isotherms. As was mentioned above, the extension of NLDFT to 2D space to determine the fluid density distribution along radial and axial directions in the cylindrical pore with smooth wall leads to solidification of a fluid in the cylindrical pore above its triple point (Ustinov and Do, 2004a). For this reason the conventional approach is not suitable for analysis of adsorption in finite pores having amorphous walls since the solidification in such pores does not occur at temperatures higher than the triple point. In this section we briefly describe a possible way of application of the NLDFT to adsorption on disordered (amorphous) materials. It should be emphasized that we rely on the same basis of the Tarazona's NLDFT version developed for one component homogeneous or inhomogeneous system in the presence of an external potential field. Very often, models for crystalline solids were applied to solve amorphous solids. Such an application is not correct as amorphous solids do give rise to disordered structure of the adsorption phase, and the distinction between the adsorption behavior in crystalline solids and that in amorphous solids must be made clear. This distinction is usually ignored in numerous applications of the NLDFT to adsorption in siliceous materials like MCM-41 and SBA-15. In such cases the quantitative description of experimental isotherms has never been achieved, and the disagreement between the model predictions and the data is attributed to a high energetic heterogeneity of those materials. From our viewpoint the latter is definitely inherent to siliceous materials, but it is not the main reason of the discrepancy between theoretical and experimental isotherms.

There are some theoretical works in which disordered solid materials are considered in the framework of quenched–annealed (QA) systems (Madden, 1992; Given, 1995; Schmidt, 2002). In this case the solid is treated as a frozen (quenched) liquid, while the fluid is represented as annealed part of the system allowed to equilibrate. Such systems are interpreted as binary mixtures of solid and fluid and their physical quantities are written as double ensemble averages. First average is performed over all degree of freedom of the fluid molecules (keeping the solid atoms fixed) and the second average is taken over the matrix. The statistical thermodynamics of such systems is rather involved. The behavior of QA systems can be described using the Rosenfeld's Fundamental Measure Theory (FMT) (Rosenfeld, 1989; Kierlik and Rosinberg, 1991), which is extended to multicomponent mixtures.

We developed an alternative method, which considers the solid–fluid interaction in a similar way that it does for the fluid–fluid interaction, that is the pair-wise

interaction potential between a solid atom and fluid molecule is split into the repulsive term accounted for by the excess Helmholtz free energy and the WCA term for the attractive forces. In doing so, we take the DFT inherent advantage to deal with disordered structures.

2.2.1. Excess Helmholtz Free Energy in the Proximity of the Solid. According to Eqs. (6), the excess Helmholtz free energy, $f_{\text{ex}}(\bar{\rho})$, increases with the increase of the dimensionless variable $\bar{\eta}$ (or the smoothed density $\bar{\rho}$). If $\bar{\eta}$ is zero the repulsive forces are also zero, which corresponds to the limiting case of rarefied gas that obeys the ideal gas law. If $\bar{\eta}$ tends to unity the excess Helmholtz free energy will tend to infinity, which corresponds to the maximum possible density $\rho_m = 6/(\pi d_{\text{HS}}^3)$. The volume in the proximity of a given point could be partly occupied by molecules of another fluid or solid atoms, which would contribute to the increasing of the excess free energy and, consequently, repulsive forces. It allows us to introduce an effective local density of a given point as follows (Ustinov and Do, 2005a). This effective local density is equal the fluid density if that point is outside the solid, and it is equal the maximum density ρ_m (instead of zero) if the point is within the solid region. Such approximation implies that fluid molecules do not penetrate to the solid due to infinitely large repulsive forces arising formally at $\rho = \rho_m$. Hence, if we do not distinguish the fluid molecules and the solid atoms in terms of their contribution to the increase of the excess Helmholtz free energy, the weight functions of Tarazona's smoothed density (Eqs. (9)) in the vicinity of the solid surface may be rewritten as follows:

$$\bar{\rho}_i(\mathbf{r}) = \int_{\text{Fluid}} \rho(\mathbf{r}')\omega_i(|\mathbf{r}-\mathbf{r}'|)\,d\mathbf{r}' + \rho_m \int_{\text{Solid}} \omega_i(|\mathbf{r}-\mathbf{r}'|)\,d\mathbf{r}', \quad i = 0, 1, 2 \tag{12}$$

If solid–fluid repulsive forces are accounted for explicitly in u^{ext}, for example, in the form of 9-3 LJ potential for the flat surface, the contribution of the solid to the excess Helmholtz free energy f_{ex} is very small. This is because the first molecular layer is formed at a distance of about one solid–fluid collision diameter from the surface, while at a shorter distance the fluid density becomes extremely small due to the repulsive term of the external potential u^{ext}. On the other hand, weight functions $\omega_0(r)$ and $\omega_2(r)$ are zero for $r > \sigma_{ff}$, and the weight function $\omega_1(r)$ is relatively small at a distance between the first molecular layer of the fluid and the surface. For this reason the conventional NLDFT and the approach accounting the contribution of the solid to the smoothed density produce nearly the same results in the case of adsorption on the crystalline surface. However, the situation drastically changes if the repulsive term of the solid–fluid interaction is accounted for *only* in the excess Helmholtz free energy, like in the case of NLDFT application to fluid–fluid interactions. In this case it is necessary to exclude the repulsive term from the LJ solid-fluid potential.

2.2.2. Attractive Solid–Fluid Potential. To exclude the repulsive term from the solid—fluid potential (as it is already accounted for in the excess Helmholtz free energy) we will use the same perturbation scheme (Weeks et al., 1971), developed for the fluid–fluid interactions. Since the both parts of the system fluid–solid are disordered, this approach is quite self-consistent. Hence, for the fluid–solid potential one can write:

$$u^{\text{ext}}(\mathbf{r}) = \int_{\text{Solid}} \phi_{sf}(|\mathbf{r}-\mathbf{r}'|)\rho_V^{(s)}\,d\mathbf{r}' \tag{13}$$

The integral is taken over the solid volume; $\rho_V^{(s)}$ is the number solid density, which is assumed to be constant. Since the free energy to be minimized is attributed only to fluid, the solid–fluid potential is considered as the external potential. In this case we do not account for the solid–fluid interaction twice, and, hence, the multiplier $\frac{1}{2}$ at the integral must be dropped. The solid–fluid pair-wise potential is given by the following equation similar to Eqs. (11):

$$\phi_{sf}(r) = \begin{cases} -\varepsilon_{sf}, & r < r_m^{(s)} \\ 4\varepsilon_{sf}[(\sigma_{sf}/r)^{12} - (\sigma_{sf}/r)^6], & r_m^{(s)} < r < r_c^{(s)} \\ 0, & r > r_c^{(s)} \end{cases} \tag{14}$$

Here ε_{sf}, and σ_{sf} are the solid–fluid potential well depth and the solid–fluid collision diameter, respectively; $r_c^{(s)}$ is the cutoff distance.

To summarize, the functional to be minimized in grand canonical ensemble is

$$\Omega = \int_{\text{Fluid}} \rho(r)[f(r) - \mu]\,dr \tag{15}$$

The condition of minimum of grand thermodynamic potential leads to the following system of equations:

$$k_B T \ln[\Lambda^3 \rho(\mathbf{r})] + f_{\text{ex}}[\bar{\rho}(\mathbf{r})] + \int_{\text{Fluid+Solid}} f'_{\text{ex}}[\bar{\rho}(\mathbf{r}')]\rho(\mathbf{r}') \frac{\partial \bar{\rho}(\mathbf{r}')}{\partial \rho(\mathbf{r})} d\mathbf{r}' + 2u^{\text{int}}(\mathbf{r}) + u^{\text{ext}}(\mathbf{r}) - \mu = 0 \quad (16)$$

where u^{int} and u^{ext} are defined by Eqs. (10) and (13), respectively. The prim at f_{ex} denotes the derivative of f_{ex} with respect to the smoothed density $\bar{\rho}$. The above equation may be solved by an iteration procedure to produce the density profile. It should be noted that Eqs. (16) is obtained with the assumption that the solid is thermodynamically inert. In terms of the attractive part of solid–fluid potential it does not introduce any difficulties as the attractive potential modeled by the WCA equation is completely accounted for in the Helmholtz free energy. This is because we drop the multiplier 1/2 in Eqs. (13). However, in the general case one must account for the change of the excess Helmholtz free energy of solid atoms in the proximity of the surface due to the change of the fluid density. It means that the minimization procedure of the grand thermodynamic potential has to be done for the whole solid—fluid system. In this case Eqs. (16) would involve an additional term associated with the derivative of the excess Helmholtz free energy of the solid with respect to the fluid density. For the sake of simplicity at present stage we assume that the excess Helmholtz free energy of the solid is constant and will address to this subtlety in our future communications.

The fluid–fluid molecular parameters d_{HS}, ε_{ff}, and σ_{ff} are determined from bulk properties and the surface tension. The solid–fluid parameters ε_{sf}, σ_{sf}, and $r_c^{(s)}$ may be determined by the least square technique using the experimental isotherm on the reference non-porous solid.

2.3. *An Example for the System Amorphous Solid Argon–Liquid Argon*

To justify the developed approach let us consider a hypothetical case when the solid has the same density as the saturated liquid argon at its boiling point and the solid atoms have exactly the same properties as those for argon molecules, which is provided by the following equalities: $\varepsilon_{ss} = \varepsilon_{sf} = \varepsilon_{ff}$, and $\sigma_{ss} = \sigma_{sf} = \sigma_{ff}$ (the hard sphere diameter and the cutoff distance are also assumed to be the same for the solid and fluid). The only difference between the solid and fluid is that one part of this system is quenched and the other one (fluid) is annealed. If we bring these two parts into contact and equilibrate at the saturation pressure no density perturbation could be observed in the proximity of the boundary between the solid and fluid, which is mathematically natural, as far as the expression for the Helmholtz free energy does not explicitly reflect whether the molecules move or remain stationary. Then the question is what density distribution could be obtained using the conventional method of the DFT application to adsorption on a crystalline surface (for simplicity this surface is assumed to be flat). In this case the fluid (liquid argon) undergoes the external field exerted by the frozen (quenched) argon, which is a specific case of adsorption. Since the density distribution in the frozen argon is uniform, the external potential may be determined by integration of the 12-6 Lennard–Jones potential over the frozen volume, which gives the following 9-3 external potential:

$$u^{\text{ext}} = \frac{2}{3}\pi\rho_L\varepsilon_{ff}\sigma_{ff}^3\left[\frac{2}{15}\left(\frac{\sigma_{ff}}{z}\right)^9 - \left(\frac{\sigma_{ff}}{z}\right)^3\right] \quad (17)$$

where ρ_L is the number density of liquid and z is the distance from the center of a given molecule to the plane passing through all frozen argon molecules lying on the outermost layer of the solid surface. Having set the external potential, the minimization of the grand thermodynamic potential Ω at the saturation pressure p_0 and the boiling point temperature leads to the density profile presented in Fig. 1(a). All calculations are performed for the set of molecular parameters taken from the paper of Neimark et al. (1998). The boundary between the "solid" (frozen or quenched argon at the liquid phase density uniformly distributed over the solid volume) and the liquid argon is denoted by the vertical dash dotted line. The dashed line to the right from the boundary is calculated with the conventional application of the NLDFT, which considers the adsorbed fluid in the external field exerted by the solid. It is seen from the figure that the fluid density corresponding to the conventional consideration shows a great oscillation, with the density being nearly zero in the proximity of the boundary. Such a behavior is unrealistic since there are no differences between the frozen and liquid argon from the viewpoint of mathematical model and we could expect the uniform density distribution in the vicinity of the boundary. The density oscillation

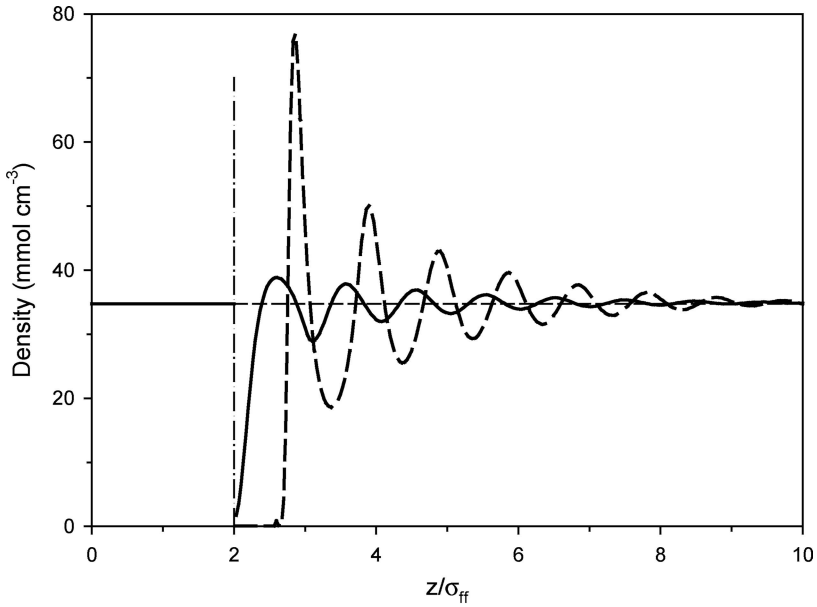

(a)

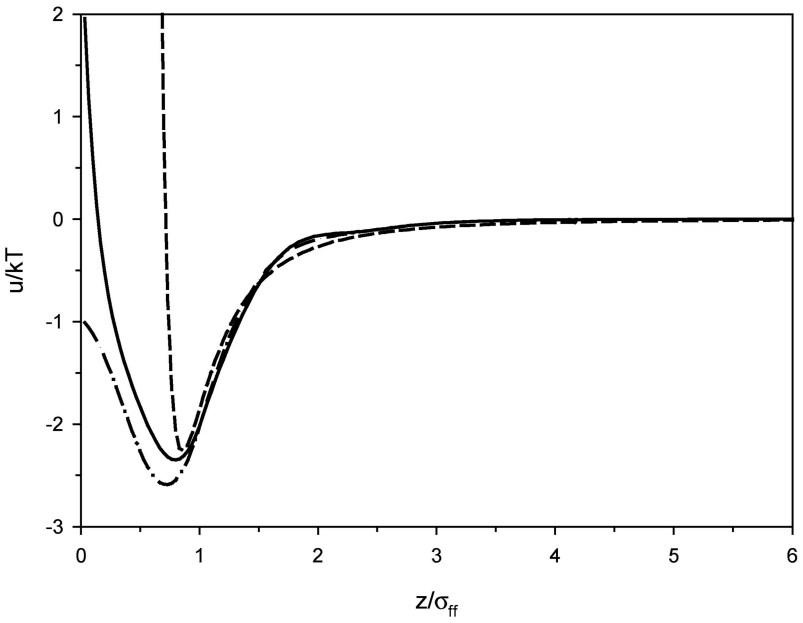

(b)

Figure 1. Quenched–annealed system for argon at its boiling point and the saturation pressure. (a) Density distribution near to the solid–liquid boundary. Vertical dash-dotted line denotes the boundary between frozen (quenched) argon (to the left) having the same density as that for the liquid argon, and annealed argon (to the right). The dashed line is plotted with the conventional NLDFT applied for the condition that the frozen argon exerts the external 9-3 LJ potential. Thin horizontal short-dashed line corresponds to the true situation when the frozen and liquid argon are brought in contact. The solid line to the right from the boundary is plotted with the developed NLDFT approach treating the solid and the fluid as a binary mixture, but the penetration of the centers of fluid molecules to the solid (beyond the dash-dotted line) is prohibited. (b) Solid–fluid potential. (Solid line) equivalent external potential at which the density distribution obtained in the conventional NLDFT is the same as in the developed approach; (dashed line) 9-3 LJ potential derived for the quenched (frozen) argon; (dash-dotted line) the equivalent external potential corresponding to the conventional NLDFT leading to the uniform density distribution (see the text).

is an artifact coming from the implicit substitution of the disordered structure of the frozen argon with its crystalline form (i.e. ordered structure). Indeed, it is implicitly assumed that centers of the outmost solid atoms are located exactly on the flat surface, which is the solid–fluid boundary, resulting in that the repulsive forces are infinitely large close to the boundary. This is the reason why the fluid density is zero on the solid surface. On the other hand, the potential minimum is the locus in the form of the plane parallel to the solid surface at a distance close to the collision diameter, which leads to the formation of a high peak of fluid density at this distance. The solid line to the right from the solid–fluid boundary shows a result of application of the approach developed in this paper. As it was described above, our model uses two simplifications, that is, (a) the fluid molecules cannot penetrate to the disordered (amorphous) solid, and (b) the excess Helmholtz free energy of the solid is not affected by the fluid. These assumptions are not completely correct (otherwise we would not obtain any density oscillation in the special case under consideration), but it seems reasonable and it makes the approach more general. It is seen from the figure that our model also leads to the decaying density oscillation, but the amplitude of the oscillation is much lower than that in the case of conventional NLDFT application. Note that the first peak of the fluid density is located exactly at a distance of half the collision diameter, i.e. closer to the amorphous solid surface compared to the conventional solution. This is a consequence of the assumption that centers of the fluid molecules cannot cross the solid–fluid boundary, but could reside directly on this boundary. Hence, it is implicitly assumed that the surface of a disordered solid material is rough in a sense that there are troughs and elevations. The consequence is that fluid molecules in the contact layer are distributed along the normal to the solid surface with variation of about one collision diameter and the maximal probability corresponding to one half of the collision diameter.

It is interesting to raise a question how the external potential exerted by the solid (the frozen argon in the case under consideration) has to change with the distance from the surface to obtain *the same* density distribution that was obtained with the developed approach? It could be easily done with the use of the same Eqs. (16), in which the smoothed density is determined by the original Eqs. (8), (9). Since the density profile for a specified bulk pressure is known from the developed approach, the unknown variable in Eqs. (16) is the effective external potential u^{ext}. This potential is plotted in Fig. 1(b) by solid line. For comparison the dashed line is calculated for the 9-3 LJ potential (Eqs. (17)). As is seen from the comparison the attractive parts of the external potential are quite close to each other. The fundamental difference lies in the repulsive part of the potential. The conventional consideration treating the solid as the crystalline one leads to an extremely sharp increase of the potential towards the solid, which prevents fluid molecules to approach the surface closer than about $0.6\ \sigma_{ff}$. In contrast to that, the developed approach leads to substantially broader potential well mainly due to dispersion of the repulsive branch of the solid–fluid potential. This dispersion reflects a fundamental distinction between amorphous and crystalline solids. Again, one could come to the conclusion that solid atoms constituting amorphous surface do not lie on the 2D plane, but are dispersed anyhow near this surface. What it means is that some fluid molecules could occupy troughs between neighboring surface atoms, while the other molecules undergo the strong repulsive forces from prominent atoms of the surface. Such a dispersion of adsorbed molecules in the contact layer could be formally described by means of the decrease of the repulsive forces exerted by the solid. The dash-dotted line in Fig. 1(b) is plotted using Eqs. (16) with the assumption that the fluid density distribution in the proximity of the surface is uniform and equal to the liquid argon density. Hence, the dash-dotted line reflects the variation of the equivalent potential exerted by the amorphous solid (or liquid) argon in the framework of the conventional NLDFT, which reproduces the homogeneous density distribution. One can see that the approximate model developed for amorphous solids leads to the equivalent solid–fluid potential (solid line), which is quite close to the exact solution (dash-dotted line). It confirms the applicability of the NLDFT based approach to describe adsorption on amorphous surfaces.

2.4. *Application of the NLDFT to the Finite Cylindrical Pore*

To calculate the density distribution in the proximity of the pore entrance we introduced the simulation cell that comprises of two parts (see the sketch in Fig. 2). One part is the cylindrical section adjacent to the pore mouth having width equal to five times the fluid–fluid collision diameter and the radius of six collision diameters

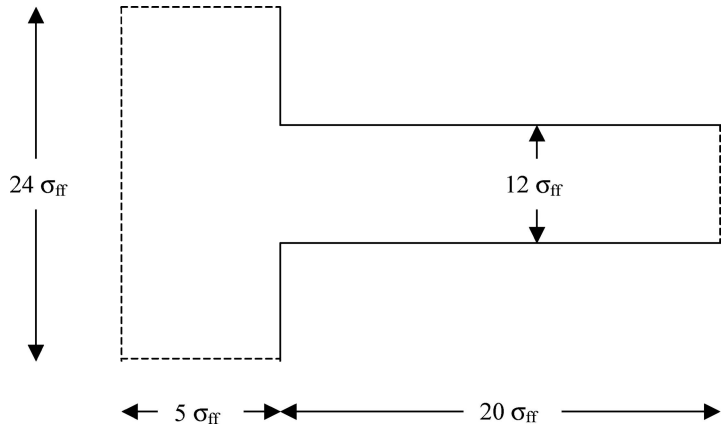

Figure 2. Scheme of the simulation cell to model argon adsorption in finite (or semi-infinite) pore accounting for the pore mouth. The mirror image boundary conditions were applied along surfaces denoted with dashed lines.

larger than the pore radius. The boundary condition for the surface opposite to the pore mouth was defined as mirror image. In the proximity of the cylindrical surface of this part of the cell we set the uniform radial density distribution, with the density outside the cell being the same as the density at the cylindrical boundary inside the cell at the same distance from the plane passing through the pore mouth. The surface boundary which is perpendicular to the pore axis was assumed to have the same properties as those for the pore wall to allow adsorption both inside the pore and on the external surface. The second part of the cell is the cylindrical section representing the inner part of the pore having a length of $20\,\sigma_{ff}$. The boundary condition on the cross-section opposite to the pore mouth was defined as a mirror image as well. The pore axis and the radius were divided into equal segments having a thickness of one tenth of the collision diameter, which means that the fluid and the solid are represented as a set of concentric rings. The mass of such a ring inside the pore is proportional to the fluid density at given radius and z-coordinate, and the mass of the solid ring is proportional to the solid density and its perimeter. For each pair of rings we defined the discrete set of Tarazona's weighted functions and that of WCA potentials as a 3-parametric function of their radii and the difference of z-coordinates.

In canonical ensemble we specified the total amount adsorbed inside the cylinder and on the external surface. The amount adsorbed was calculated only inside the cylinder to exclude the contribution of the adsorption on the external surface as its area is chosen arbitrarily. Also, we determined the amount adsorbed on the internal boundary. Since this boundary is far away from the pore mouth, one should expect that the amount adsorbed determined for this cross-section coincides with that for the infinite cylindrical pore.

3. Results

3.1. Argon Adsorption on Non-porous Silica and MCM-41 at 87.3 K

Adsorption of nitrogen and argon on non-porous silica and in cylindrical pores of MCM-41 silica is a special issue, which is considered elsewhere in details (Ustinov et al., 2005b, 2005c). In this section we present briefly the result of application of 1D version of the new approach to argon adsorption on the flat and cylindrical surface of infinitely long pores of MCM-41 samples for the purpose to show how the solid–fluid parameters were determined. All molecular parameters are presented in Table 1.

The fluid–fluid parameters were taken from the paper of Neimark et al. (1998). The number density of silica was determined from the value 2.2 g/cm^3 accounting for both silica and oxygen atoms. The solid–fluid potential well depth ε_{sf}/k_B, the solid–fluid collision diameter σ_{sf}, and the cutoff distance $r_c^{(s)}$ were determined by the least square technique using the argon adsorption isotherm on non-porous silica LiChrospher Si-1000 at 87.3 K (Kruk and Jaroniec, 2000). It should be noted that the parameters depend on the specific surface area of this sample. The uncertainty of the BET estimation of this area is of about 35 percents, with the BET

Table 1. Molecular parameters for the system Ar–silica surface.

	ε_{ff}/k_B (K)	σ_{ff} (nm)	d_{HS} (nm)	ε_{sf}/k_B (K)	σ_{sf} (nm)	$r_c^{(s)}/\sigma_{sf}$	$\rho_V^{(s)}$ (nm^{-3})
Ar	118.05	0.3305	0.3380	95.60	0.3127	4.5	66.15

surface being between 18 and 26 m^2/g (Jaroniec et al., 1999). Interestingly, it does not matter what value of surface area is chosen, the correlation of the experimental isotherm is equally good, but the set of solid–fluid parameters is different for different choice of surface area. To correctly choose the proper set, we have to rely on the data of the condensation/evaporation pressure dependence on the pore diameter (Kruk and Jaroniec, 2000). We found that the experimental dependence of condensation pressure on the pore diameter is excellently described by the theoretical dependence obtained for the equilibrium transition pressure if the solid–fluid molecular parameters are determined for the LiChrospher specific surface area of 24 m^2/g. The same surface area we obtained for nitrogen adsorption data, as well. Thus we conclude that the adsorption branch of the isotherm corresponds to the true equilibrium and that the solid–fluid molecular parameters listed in Table 1 corresponding to the value 24 m^2/g are correct values.

Figure 3 shows the argon adsorption isotherm on non-porous silica LiChrospher Si-1000 at 87.3 K. As is seen from the figure, the description of the experimental isotherm is nearly excellent both in the liner and logarithmic scales. For comparison we also present the results obtained from the application of the conventional DFT as the dashed line. In this conventional DFT we use the 10-4 LJ solid–fluid potential for the interaction of argon molecules with the silica surface oxygen atoms using the parameters reported by Neimark and Ravikovitch (2001). The comparison of the curves is a convincing proof of a high reliability of the developed approach presented in this paper. We also investigated a sensitivity of the results to variation of the solid–fluid molecular parameters. In the first case we increased the solid–fluid potential well depth ε_{sf} by 5 percents, keeping the same solid–fluid collision diameter. The corresponding calculated isotherm is shown in Fig. 3 with dash-dotted line. In the second case the group $\varepsilon_{sf}{\sigma_{sf}}^3$ was kept constant, but the solid–fluid collision diameter was increased by 5 percents (dash-double dotted line). The figure shows that the sensitivity of the results to the molecular parameters is quite large, which makes the set of the found parameters sufficiently reliable.

3.2. *Modeling of Argon Adsorption in Infinite Cylindrical Pore of MCM-41 at 87.3 K*

The relation between the condensation and evaporation pressures and the pore diameter is presented in Fig. 4 for the system Ar – MCM-41 silica at 87.3 K. The pore diameters were determined independently using XRD data (Kruk et al., 1997a; 1997b; Dabadie et al., 1996). The solid line is the prediction of the equilibrium transition pressure versus diameter, obtained using the developed version of NLDFT with the solid–fluid parameters listed in Table 1, which correspond to the choice of the specific surface area of non-porous silica LiChrospher Si-1000 of 24 m^2/g.

As an example, we present in Fig. 5 a comparison of experimental argon adsorption isotherm (only adsorption branch) at 87.29 K in an MCM-41 silica sample (Kruk and Jaroniec, 2000) with the prediction performed with the developed and the conventional NLDFT models. The pore diameter of the sample designated as (4.2) determined with XRD technique is 4.2 nm. Solid line is the prediction using the new method of application of the NLDFT to amorphous solids for the pore diameter 4.13 nm. Dashed line is calculated by the conventional approach for the same diameter. However, in this case the value 4.13 nm was considered as the diameter available for the fluid molecules (so called physical diameter), so the geometrical diameter defined as the distance between centers of opposite surface solid atoms was taken by the solid–fluid collision diameter larger, i.e. $4.13 + 0.3 = 4.43$ nm. It is seen from the figure that the conventional NLDFT approach leads to pronounced layering, which is not observed experimentally as well as by the approach developed in this paper.

3.3. *Modeling of Argon Adsorption in Finite Cylindrical Pore of MCM-41 at 87.3 K*

Having developed the model as applied to one-dimensional tasks like the adsorption on non-porous silica and infinite cylindrical pores, we now turn to

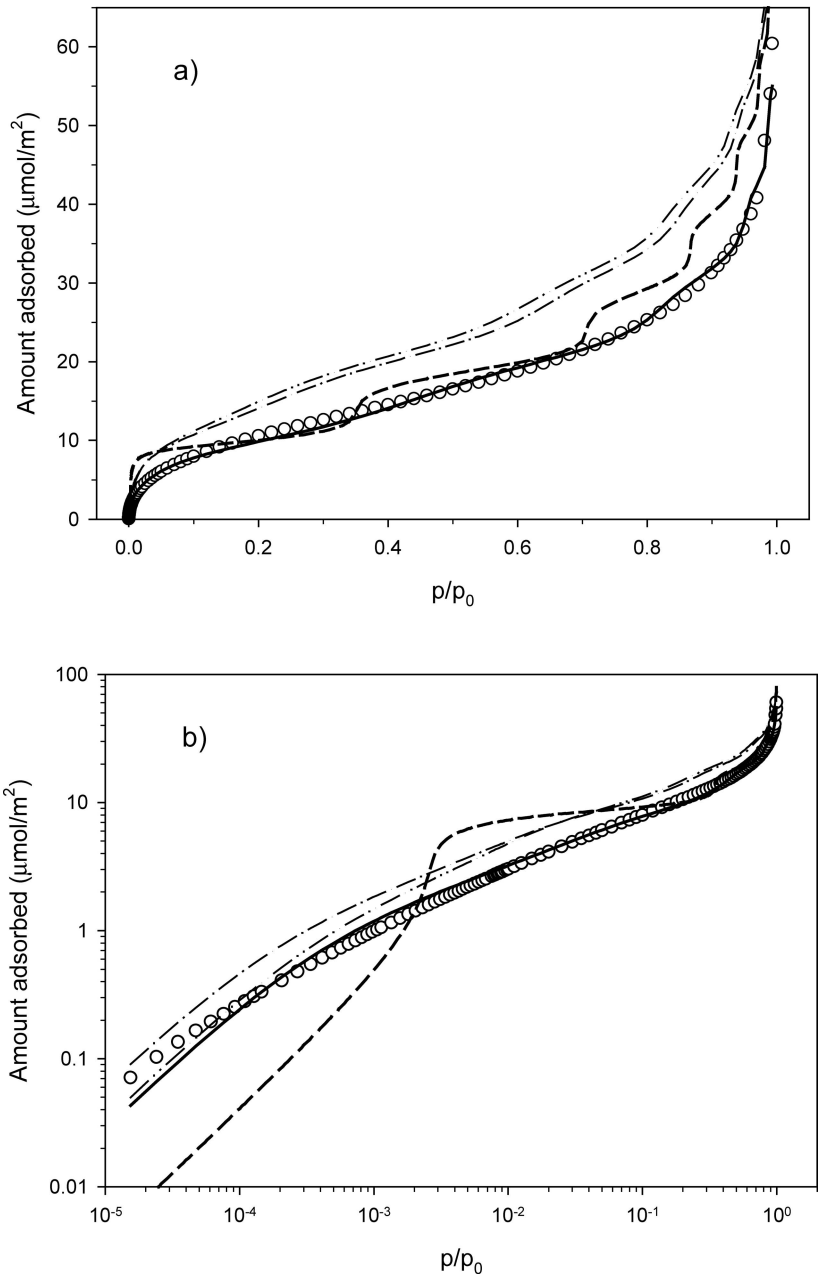

Figure 3. Argon adsorption isotherm on silica LiChrospher Si-1000 at 87.29 K in linear scale (a) and logarithmic scale (b). (Circles) experimental data (Kruk and Jaroniec, 2000); (solid line) the developed version of NLDFT for amorphous surface; (dashed line) the conventional NLDFT. The dash-dotted line is plotted for the increased value of the solid–fluid potential well depth ε_{sf} by 5 percents. The dash-double dotted line is for the increased solid–fluid collision diameter by 5 percents keeping the group $\varepsilon_{sf}\sigma_{sf}{}^3$ constant.

analysis of argon adsorption in the finite cylindrical pore. This is a two-dimensional task, in which we can obtain in details information about the density variation both axially and radially.

3.3.1. Finite Pores in Canonical Ensemble. In Fig. 6 we present the adsorption isotherm in the finite pore, having a diameter of 4 nm. As it was mentioned above, the amount adsorbed is determined as the integral of

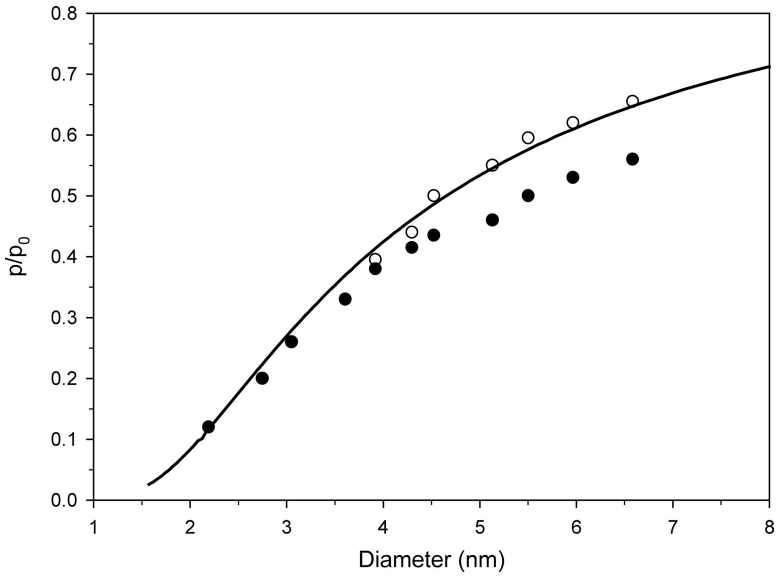

Figure 4. Experimental dependence of the capillary condensation pressure (open circles) and the capillary evaporation pressure (filled circles) on the pore diameter for the system ArMCM-41 at 87.3 K (Kruk and Jaroniec, 2000). The solid line is calculated for the equilibrium transition pressure by the developed approach for the solid–fluid parameters corresponding to the surface area of nonporous silica of 24 m^2/g.

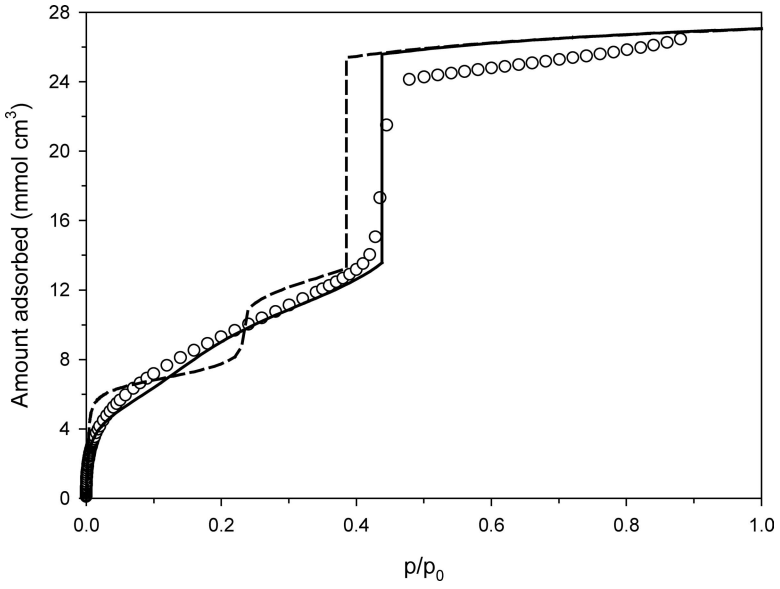

Figure 5. Experimental argon adsorption isotherm (adsorption branch) at 87.29 K in a sample MCM-41 designated in (Kruk and Jaroniec, 2000) as (4.2). The solid line is calculated with the developed NLDFT approach for amorphous solids for the pore diameter of 4.13 nm. The dashed line is plotted with the conventional NLDFT for the solid–fluid molecular parameters reported in Neimark et al. (1998). In both cases the phase transition corresponds to the equilibrium transition pressure.

the argon density over the pore volume included to the simulation cell. The length of this cylindrical section is 20 times the collision diameter (6.61 nm). The part *OAGB* of the isotherm corresponds to the liquid-like film wetting the pore walls, with the *AGB* section being the metastable adsorption branch of the isotherm. Point *B* is the vapor-like spinodal point where the liquid film loses its mechanical stability, and at this point the

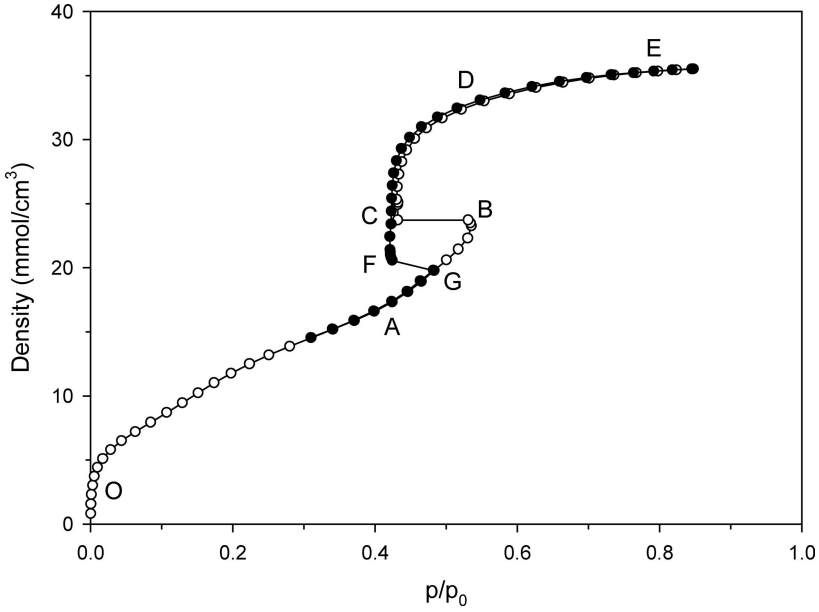

Figure 6. Theoretical argon adsorption isotherm in the finite cylindrical pore of 4 nm diameter for the developed version of canonical NLDFT. Filled points and open points denote the adsorption and desorption branch, respectively. Explanations are in the body.

configuration of adsorbed film switches to one that possesses two coexisting phases. The bulk pressure jumps to the point *C*, corresponding to the equilibrium between the liquid-like phase filling the core of the pore and the gas-like phase closer to the pore mouth. Further increase of the amount adsorbed leads to a small increase the equilibrium bulk pressure. But as the meniscus advances toward the pore mouth where the potential field exerted by the solid is less than that away from the pore mouth, the bulk pressure increases faster to compensate for this low solid–fluid potential field. We did not approach the saturation pressure to avoid the condensation in the section of simulation cell outside the pore, which would lead to blocking the pore by liquid. The decrease of the amount adsorbed (filled circles) is accompanied by the decrease of the bulk phase pressure, with the isotherm being nearly reversible along the part *EDC*. Upon further decrease of the amount adsorbed from the point *C*, we observe that the bulk pressure remains nearly constant up to the point *F*. At this point the liquid-like phase completely evaporates from the central part of the pore leading to the configuration of adsorbed film adjacent to the pore wall and the gas-like phase spanning the whole core of the pore. Since the two phase coexistence disappears, the pressure jumps to the point *G*, which is on the metastable section of the adsorption branch of the isotherm. Further decrease of the amount adsorbed is reversible with respect to the adsorption branch *OAGB*. Figure 7 shows the density distributions in the finite pore for different amounts adsorbed on adsorption and desorption branches of the isotherm. At the vapor-like spinodal pressure (point *B* on the isotherm depicted in Fig. 6) the adsorbed phase is the liquid-like film covering the internal pore wall surface and the outer surface (Fig. 7(a)). It is seen that the film thickness inside the pore is larger than that at the external surface due to the enhancement of the solid – fluid potential inside the pore and, what is more important, because the liquid – vapor interface tends to be smaller, which causes the thickening of the liquid film. The spinodal point is the limiting case of mechanical stability of the liquid film. A small increase of the amount adsorbed leads to the split of the nearly homogeneous phase into two coexisting phases (Fig. 7(b), point *C* in the isotherm). It is important to note that such a split was not observed in the case of infinite pore regardless whether we used one-dimensional or two-dimensional version of the DFT. In the latter case some nucleation were needed, which we achieved by introducing the energetic heterogeneity of the pore wall. In the case of finite pore the spontaneous appearance of the liquid phase in the core of the pore was always observed at the vapor-like spinodal point no matter how long is the simulation

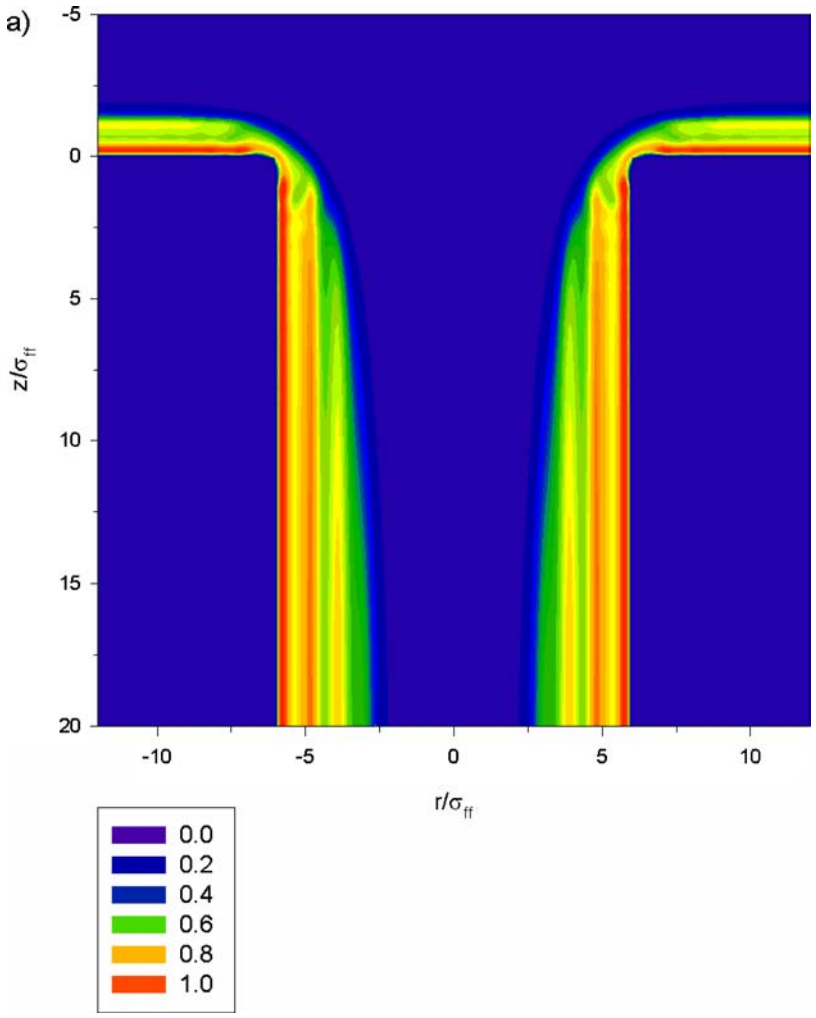

Figure 7. Argon density distribution in the finite cylindrical pore of 4 nm diameter. Different plots correspond to following points of the isotherm depicted in Fig. 6: (a) – *B*; (b) – *C*; (c) – *D*; (d) – *F*; (e) – *G*. Contour lines are defined for the specified reduced density $\rho\sigma_{ff}^3$, where ρ is the number argon density, nm^{-3}. The reduced density of liquid argon is 0.76. *(Continued on next page.)*

cell. It means that the pore entrance may act as a nucleation site. Once the condensation has occurred, some amount of the adsorbed fluid moves from the neighborhood of the pore mouth to the central part of the pore to achieve lower potential energy. By this reason the film thickness on the external surface and in the vicinity of the pore mouth inside the pore becomes thinner, which corresponds to the smaller equilibrium bulk pressure. This is the reason why the pressure jumps from the spinodal pressure to the point *C* on the isotherm corresponding to the equilibrium transition pressure. Further increase of the amount adsorbed leads to the movement of the nearly semispherical meniscus dividing the two coexisting phases toward the pore mouth. For the first period the bulk pressure remains nearly constant and equal to the equilibrium transition pressure. However, as the meniscus approaches the pore entrance, it falls into the region where the potential exerted by the solid is smaller. It leads to the gradual increase of the bulk pressure, which becomes sharper as the meniscus is closer to the pore entrance. At point *D* the pressure is the same as that for the spinodal point *B*. Figure 7(c) presents the argon density distribution at this point. In the open pore (grand canonical) when the bulk pressure is specified after the spinodal point is reached the amount adsorbed suddenly increases corresponding to

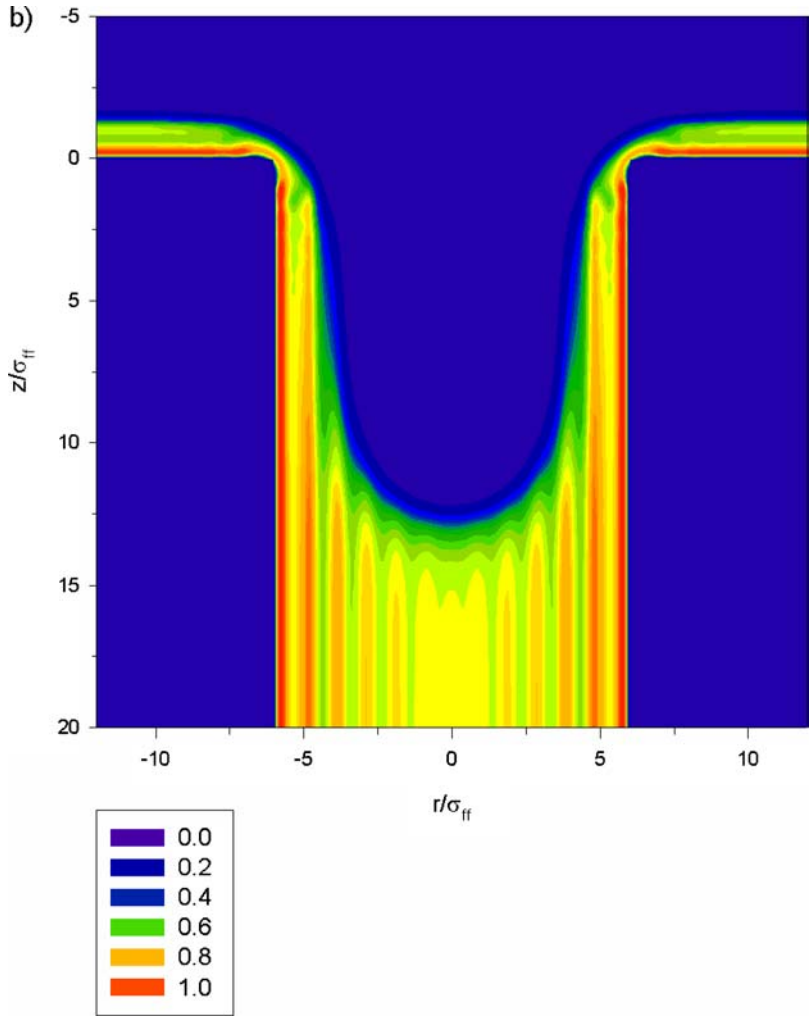

Figure 7. (Continued).

the transition from the point *B* to the point *D*. Hence, the sequence of Fig. 7(a) and (c) shows what happens inside the pore at the pressure of the spinodal condensation.

During the decrease of the amount adsorbed the meniscus moves toward the center of the pore. When the meniscus is sufficiently far away from the pore mouth the bulk pressure becomes nearly constant and equal to the equilibrium transition pressure. Since the simulation cell is finite in length with mirror-image boundary conditions, the central part of the pore is a finite bridge spanning from the meniscus to its mirror image. If the bridge is sufficiently thin, it loses its mechanical stability and disappears. It can be observed in the point *F* of the isotherm for which the density distribution is shown in Fig. 7(d). At this point the width of the bridge is about 4.2 collision diameters, that is, about 1.3 nm. Once the bridge is destroyed, the pressure suddenly increases, and the system moves from point *F* to point *G* of the isotherm. At this point *G* the density distribution is shown in Fig. 7(e). Note that the increase of the length of the cell leads to the decrease of the specific amount adsorbed at which the bridge disappears. This is because the contribution of the mass accumulated in the bridge at the point of the limit of its stability to the total amount adsorbed in the whole pore volume in this case decreases. Hence, in the limiting case of infinitely long pore the desorption branch of the isotherm lies on the curve *EDCA*, with the complete evaporation exactly corresponding to the equilibrium transition pressure. Consequently, modeling of

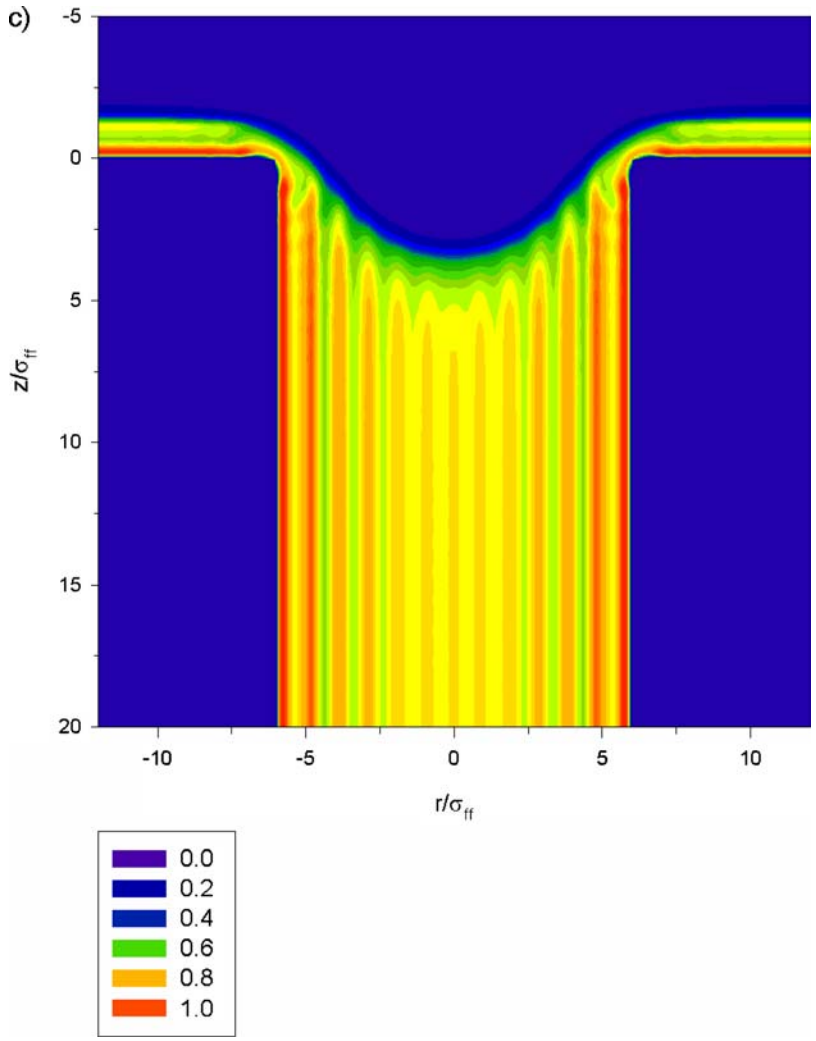

Figure 7. (Continued).

adsorption in the cylindrical pore (no matter how long it is) accounting for the pore entrance unambiguously supports the classical scenario that the capillary condensation occurs at the vapor-like spinodal pressure, which is the upper limit of mechanical stability of the metastable adsorption branch of the isotherm, while the capillary evaporation occurs at the equilibrium transition pressure via receding of the menisci toward each other.

The considered mechanism of adsorption in the finite pore allows us to reconstruct the isotherm for the case of infinitely long cylindrical pore. In the central part of the pore far away from its mouth the density distribution along the pore axis is homogeneous. Consequently, the amount adsorbed determined in the section of the pore, far away from the pore entrance must be the same as that in the infinite pore of the same size. Argon adsorption isotherms calculated with the canonical version of NLDFT for semi-infinite pores of different diameter accounting for the pore mouth are presented in Fig. 8. Open and filled symbols denote the adsorption and desorption branches of isotherms, respectively. All adsorption branches terminate at corresponding spinodal points, and upon a minute addition of adsorbate the pressure sharp jumps from vapor-like spinodal point to equilibrium transition pressure, at which coexisting phases exist. Desorption branches terminate at the equilibrium transition pressures. Vertical dashed lines designate the evaporation pressure, which always coincides with the equilibrium transition

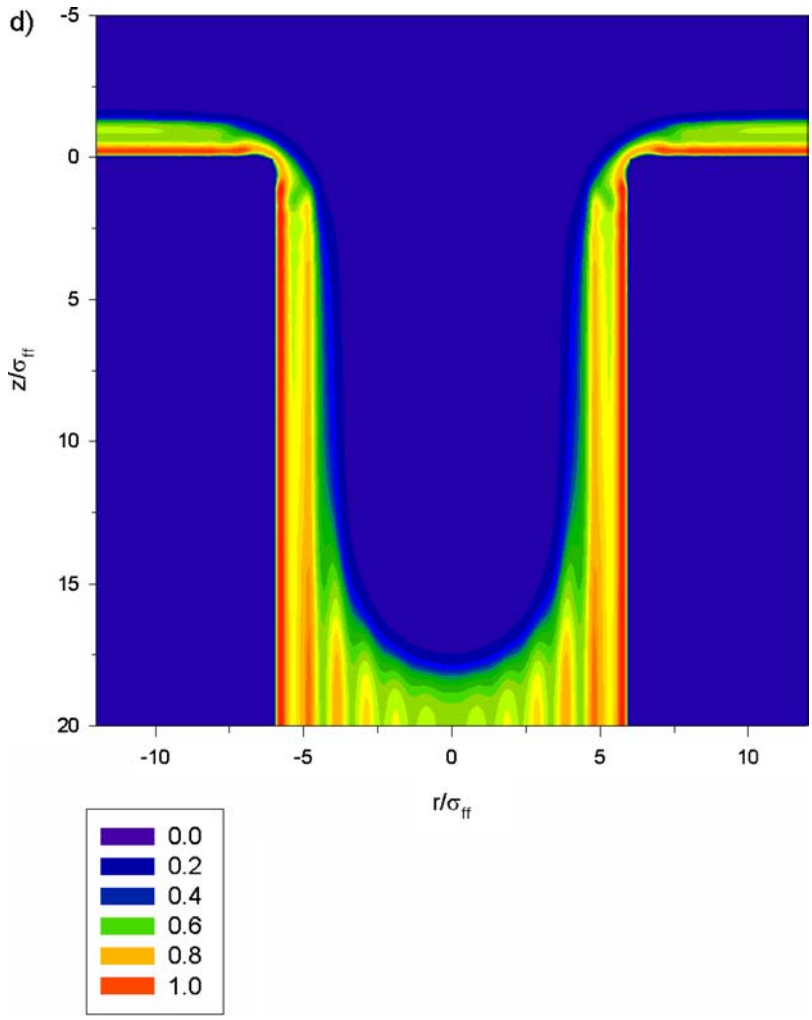

Figure 7. (Continued).

pressure. Horizontal dashed lines designate the split of the liquid-like film homogeneously covered the pore wall surface into two sections, which occurs at the vapor-like spinodal point. The new phase appeared in the central part of the pore is the liquid-like fluid filling all pore volume in this section. The second phase is the liquid-like film coexisting with the vapor in the core of the pore. The two sections are separated by the semispherical meniscus that once appeared starts moving towards the open ends of the pore with an increase of the amount adsorbed. Solid lines in the figure are obtained with the same model of two-dimensional NLDFT applied to the infinite pore. In this case the pore entrance was not accounted for and the simulation cell was a section of the infinite pore, with the boundary conditions at the two ends of the simulation cell are those of mirror images. In this case the density distribution was homogeneous along the pore axis irrespective of the amount adsorbed in the simulation cell, which is equivalent to the case of the one-dimensional NLDFT accounted for only radial density distribution. As is seen from the figure, for pores larger than 2 nm the isotherm calculated for the infinite pore has the backward part between the vapor-like and the liquid-like spinodal points. However, in reality such a scenario cannot be realized due to the presence of the pore mouth. During adsorption the pore mouth inevitably nucleates the condensation at the vapor-like spinodal pressure, leading to the appearance of the two phases, which can coexist only at the equilibrium transition

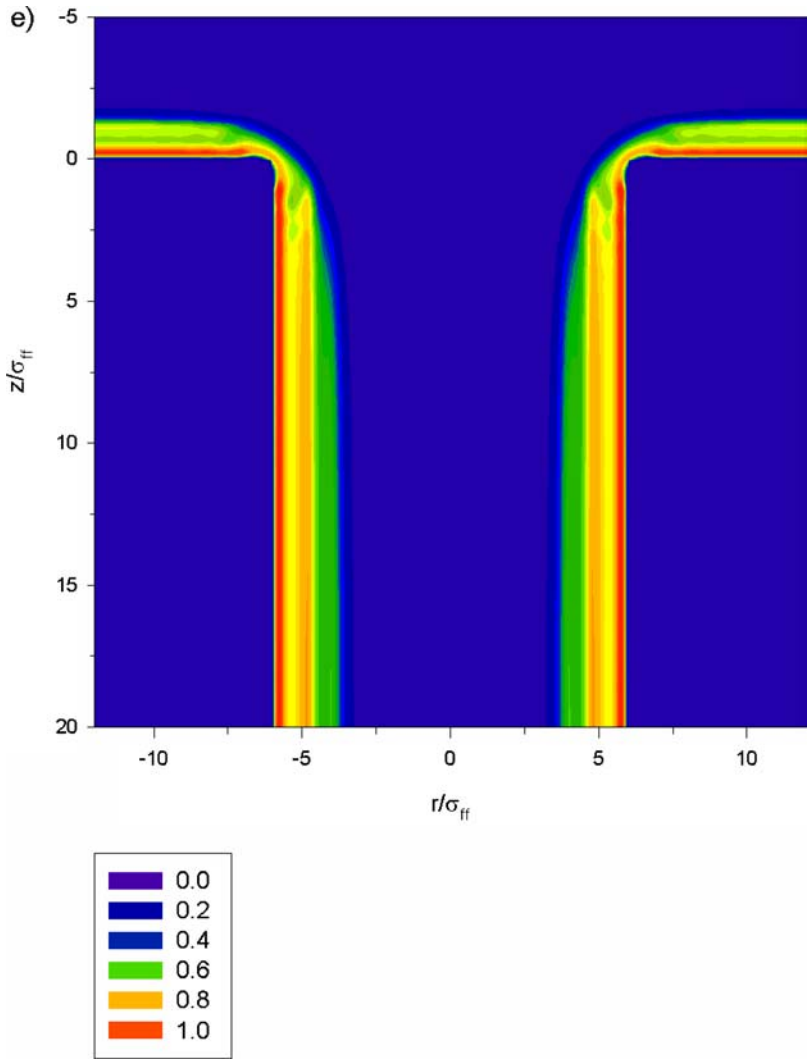

Figure 7. (Continued).

pressure. During the desorption the menisci start receding from the open ends of the pore exactly at the equilibrium transition pressure, with this pressure remaining constant until all liquid-like phase is evaporated from the core of the pore. Note that the spinodal points appear for pores larger than 2 nm. It means that the dependence of condensation/evaporation pressure on the pore diameter predicted by the developed version of the NLDFT is reversible for pores smaller than 2 nm, which is an agreement with the result obtained with the conventional NLDFT. It should be also noted that the isotherms obtained with the 2D DFT accounting for the pore entrance and those corresponding to the one-dimensional task for the infinitely long pore completely coincide for the adsorption branch up to the vapor-like spinodal point and for the desorption branch down to the equilibrium transition pressure, which confirms the correctness of the applied technique.

3.3.2. Finite Pores in Grand Canonical Ensemble. Experimentally adsorption isotherms are measured at specified values of the bulk pressure. This situation corresponds to the grand canonical ensemble, which implies that the pore is allowed to exchange mass with the surrounding via the open pore ends. Let the bulk pressure be the vapor-like spinodal pressure and imagine that the mass transfer through the pore mouth is much slower than any rearrangement of the density

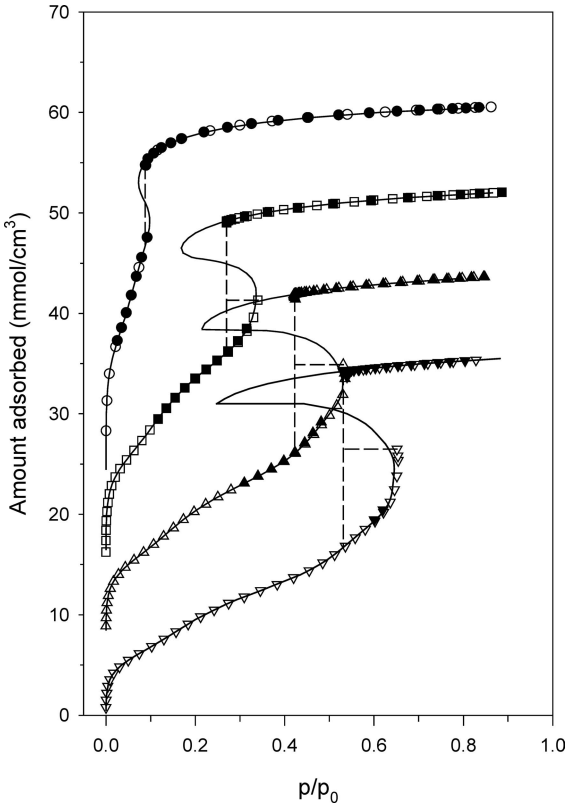

Figure 8. Argon adsorption isotherms calculated with the canonical NLDFT version accounting for the pore mouth of semi-infinite cylindrical pores at the following pore diameters (nm): 2 (circles), 3 (squares), 4 (triangles up), and 5 (triangles down). Open and filled signs denote adsorption and desorption branch of the isotherm, respectively. The amounts adsorbed for diameter 4, 3, and 2 nm are incremented by 8, 16, and 24 mmol/cm^3, respectively. Solid lines are plotted with the canonical NLDFT for infinite pores. Horizontal dashed lines denote the spontaneous condensation in the central part of the closed pore as a result of redistribution of the adsorbed fluid with the appearance of liquid-like and vapor-like coexisting phases. Vertical dashed lines denote the spontaneous evaporation at the equilibrium transition pressure.

distribution inside the pore. Such an assumption is reasonable if the length of the pore is sufficiently large. It allows us to assume that the sudden density redistribution associated with the capillary condensation in the pore occurs at a specified total amount of the fluid, i.e., in the canonical ensemble. As it was shown in the previous section, the capillary spinodal condensation leads to the sharp decrease of pressure from that at the vapor-like spinodal point to the equilibrium bulk phase. However, since the actual pressure in the bulk phase is kept the same as that for the spinodal point (i.e., greater than the equilibrium transition pressure) in the canonical ensemble, the additional amount of the fluid will enter the pore through its ends until the system comes to the global equilibrium, corresponding to the completely filled pore. We provided computations in the grand canonical ensemble with the same 2D NLDFT version for the finite pore of 5 nm to illustrate the equivalence of the results obtained in the canonical and grand canonical ensemble (which is, of course, expected, since the Helmholtz free energy defined in the canonical and grand canonical ensembles are supposed to be the same). The isotherm is presented in Fig. 9. In this case the amount adsorbed is calculated as the average density inside the simulation cell between its inner boundary and the pore mouth. It is seen from the figure that the capillary condensation occurs exactly at the vapor-like spinodal pressure determined with the canonical NLDFT. The desorption branch calculated by the grand canonical NLDFT coincides with that obtained by the canonical NLDFT for the finite pore. The capillary evaporation corresponds to the equilibrium transition pressure. Below this pressure the adsorption branch coincides with the desorption branches of the isotherm. Thus, both the canonical and the grand canonical versions of the NLDFT lead to the classical scenario that the capillary condensation in the cylindrical pore with open ends occurs at the vapor-like spinodal pressure, which is the upper limit of the metastable adsorption branch of the isotherm, while the capillary evaporation occurs at the equilibrium transition pressure via a mechanism of receding menisci from the pore ends. Thus, in this paper we showed that in the framework of 2D non-local density functional theory there are no any additional peculiarities associated with the pore entrance. At the same time, the problem of reversibility, the closure point of the hysteresis loop and seemingly equilibrium adsorption branch of the isotherm needs further efforts.

Conclusions

We considered the mechanism of capillary condensation and evaporation in the cylindrical silica-like pore with open ends by means of the two-dimensional non-local density functional theory. The pore silica surface is amorphous and the solid-fluid interaction is determined in the same framework as done for the fluid-fluid interaction. This is one of the important points of the paper, and with this approach we are able to describe the adsorption on non-porous surface extremely well. Such an excellent agreement between the DFT results

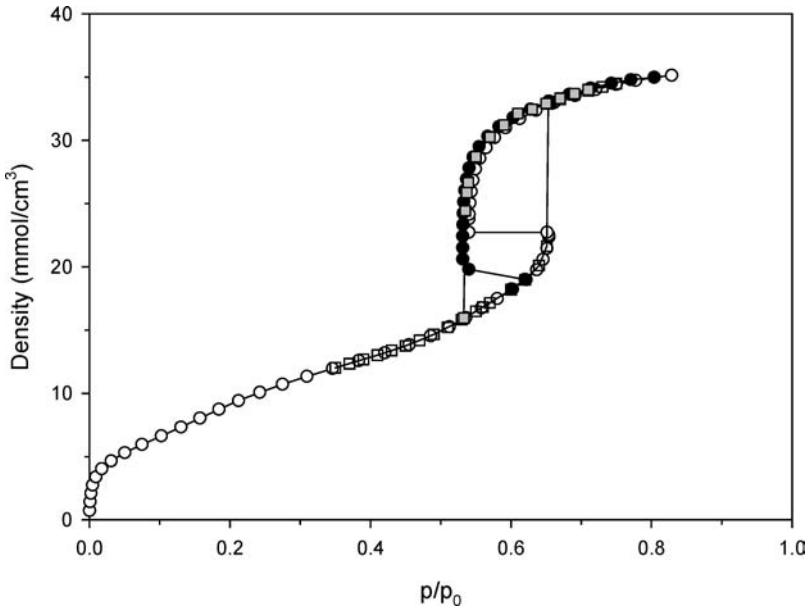

Figure 9. Calculated argon adsorption isotherm in the finite cylindrical pore of 5 nm at 87.3 K. Black and grey signs correspond to the canonical (close pore) and the grand canonical ensemble (open pore), respectively. Open signs denote the adsorption and filled signs denote desorption. The figure shows that the isotherms calculated with the canonical and grand canonical NLDFT versions are in complete agreement. The capillary condensation pressure determined in the grand canonical ensemble is the vapor-like spinodal pressure determined in canonical ensemble. The capillary evaporation pressure corresponds to the equilibrium transition pressure.

and experimental data was never possible if the surface is treated as a crystalline surface. The density distribution was determined in the proximity of the pore mouth along the adsorption and desorption branches of the isotherm accounting for the adsorption on the external surface at passing through the pore entrance. The analysis of the hysteresis phenomenon has been done with the canonical and grand canonical NLDFT. Both versions of the NLDFT support the classical scenario that the capillary condensation occurs at the vapor-like spinodal pressure and the evaporation occurs at the equilibrium transition pressure via receding of the menisci from the pore ends.

Acknowledgment

Support from the Australian Research Council is gratefully acknowledged.

References

Barrett, E.P., L.G. Joyner, and P.P. Halenda, "The Determination of Pore Volume and Area Distributions in Porous Substances. I. Computations from Nitrogen Isotherms," *J. Am. Chem. Soc.*, **73**, 373–380 (1951).

Beck, J.S., J.C. Vartuli, W.J. Roth, M.E Leonowicz, C.T. Kresge, K.D. Schmitt, C. T-W. Chu, D.H. Olson, E.W. Sheppard, S.B. McCullen, J.B. Higgins, and J.L. Schlenker, "A New Family of Mesoporous Molecular Sieves Prepared with Liquid Crystals Templates," *J. Am. Chem. Soc.*, **114**, 10834–10843 (1992).

Bhatia, S.K. and C.G. Sonwane, "Capillary Coexistence and Criticality in Mesopores: Modification of the Kelvin Theory," *Langmuir*, **14**, 1521–1524 (1998).

Branton, P.J., P.G. Hall, and K.S. W. Sing, "Physisorption of Nitrogen and Oxygen by MCM-41, A Model Mesoporous Adsorbent," *J. Chem. Soc., Chem. Commun.*, 1257–1258 (1993).

Broekhoff, J.C. P. and J.H. de Boer, "Pore Systems in Catalysts. IX. Calculation of Pore Distributions from the Adsorption Branch of Nitrogen Sorption Isotherms in the Case of Open Cylindrical Pores. 1. Fundamental Equations," *Journal of Catalysis*, **9**, 8–14 (1967a).

Broekhoff, J.C. P. and J.H. de Boer, "Pore Systems in Catalysts. X. Calculations of Pore Distributions from the Adsorption Branch of Nitrogen Sorption Isotherms in the Case of Open Cylindrical Pores. 2. Applications," *Journal of Catalysis*, **9**, 14–27 (1967b).

Broekhoff, J.C. P. and J.H. de Boer, "Pore Systems in Catalysts. XII. Pore Distributions From the Desorption Branch of a Nitrogen Sorption Isotherm in the Case of Cylindrical Pores. 1. An Analysis of the Capillary Evaporation Process," *Journal of Catalysis*, **10**, 368–376 (1968a).

Broekhoff, J.C. P. and J.H. de Boer, "Pore Systems in Catalysts. XIII. Pore Distributions from the Desorption Branch of a Nitrogen Sorption Isotherm in the Case of Cylindrical Pores. 2. Applications," **10**, 377–390 (1968b).

Broekhoff, J.C. P. and J.H. de Boer, "Pore Systems in Catalysts. XIV. Calculation of the Cumulative Distribution Functions for Slit-Shaped Pores from the Desorption Branch of a Nitrogen Sorption Isotherm," **10**, 391–400 (1968c).

Burgess, C. G., D.H. Everett, and H. Douglas, "Lower Closure Point in Adsorption Hysteresis of the Capillary Condensation Type," *J. Colloid Interface Sci.*, **33**, 611–614 (1970).

Carnahan, N.F. and K.E. Starling, "Equation of State for Nonattracting Rigid Spheres," *J. Chem. Phys.*, **51**, 635–636 (1969).

Dabadie, T., A. Ayral, C. Guizard, L. Cot, and P. Lacan, "Synthesis and Characterization of Inorganic Gels in a Lyotropic Liquid Crystal Medium. 2. Synthesis of Silica Gels in Lyotropic Crystal Phases Obtained from Cationic Surfactants," *J. Mater. Chem.*, **6**, 1789–1794 (1996).

Evans, R., U.M.B Marconi, and P. Tarazona, "Capillary Condensation and Adsorption in Cylindrical and Slit-Like Pores," *J. Chem. Soc., Faraday Trans. 2*, **82**, 1763–1787 (1986).

Everett, D.H. In *The Solid–Gas Interface*; Flood, E.A., Ed.; Marcel Dekker: New York, 1967; Vol. 2, Chap. 36, p. 1055.

Franke, O., G. Schulz-Ekloff, J. Rathousky, J. Starek, and A. Zukal, "Unusual Type of Adsorption Isotherm Describing Capillary Condensation Without Hysteresis," *J. Chem. Soc., Chem. Commun.*, 724–726 (1993).

Gelb, L.D., "The Ins and Outs of Capillary Condensation in Cylindrical Pores," *Mol. Phys.*, **100**, 2049–2057 (2002).

Given, J.A., "On the Thermodynamic of Fluids Adsorbed in Porous Media," *J. Chem. Phys.*, **102**, 2934–2945 (1995).

Gonzalez, A., J.A. White, F.L. Roman, and S. Velasco, "Density Functional Theory for Small Systems: Hard Spheres in a Closed Spherical Cavity," *Phys. Rev. Lett.*, **79**, 2466–2469 (1997).

Greg, S.J. and K.S. W. Sing, *Adsorption, Surface Area and Porosity*; Academic Press: London, 1982.

Heffelfinger, G.S., F. van Swol, and K.E. Gubbins, "Adsorption Hysteresis in Narrow Pores," *J. Chem. Phys.*, **89**, 5202–5205 (1988).

Inoue, S., Y. Hanzawa, and K. Kaneko, "Prediction of Hysteresis Disappearance in the Adsorption Isotherm of N_2 on Regular Mesoporous Silica," *Langmuir*, **14**, 3079–3081 (1998).

Jaroniec, M., M. Kruk, and J.P. Olivier, "Standard Nitrogen Adsorption Data for Characterization of Nanoporous Silicas," *Langmuir*, **15**, 5410–5413 (1999).

Kadlec, O. and M.M. Dubinin, "Limits of Applicability of the Mechanism of Capillary Condensation," *J. Colloid Interface Sci.*, **31**, 479–489 (1969).

Kierlik, E. and M.L. Rosinberg, "Density Functional Theory for Inhomogeneous Fluids: Adsorption of Binary Mixtures," *Phys. Rev. A*, **44**, 5025–5037 (1991).

Kresge, C.T., M.E. Leonowicz, W.J. Roth, J.C. Vartuli, and J.S. Beck, "Ordered Mesoporous Molecular Sieves Synthesized by a Liquid-Crystal Template Mechanism," *Nature*, **359b** 710–712 (1992).

Kruk, M., M. Jaroniec, and A. Sayari, "Adsorption Study of Surface and Structural Properties of MCM-41 Materials of Different Pore Sizes," *J. Phys. Chem. B.*, **101**, 583–589 (1997a).

Kruk, M., M. Jaroniec, and A. Sayari, "Structural and Surface Properties of Siliceous and Titanium-Modified HMS Molecular Sieves," *J. Microporous Mater.*, **9**, 173–183 (1997b).

Kruk, M., M. Jaroniec, and A. Sayari, "Application of Large Pore MCM-41 Molecular Sieves to Improve Pore Size Analysis Using Nitrogen Adsorption Measurements," *Langmuir*, **13**, 6267–6273 (1997c).

Kruk, M., M. Jaroniec, and A. Sayari, "Nitrogen Adsorption Study of MCM-41 Molecular Sieves Synthesized Using Hydrothermal Restructuring," *Adsorption*, **6**, 47–51 (2000).

Kruk, M. and M. Jaroniec, "Accurate Method for Calculating Mesopore Size Distributions From Argon Adsorption Data at 87 K Developed Using Model MCM-41 Materials," *Chem. Mater.*, **12**, 222–230 (2000).

Kruk, M. and M. Jaroniec, "Gas Adsorption Characterization of Ordered Organic—Inorganic Nanocomposite Materials," *Chem. Mater.*, **13**, 3169–3183 (2001).

Kruk, M. and M. Jaroniec, "Determination of Mesopore Size Distributions From Argon Adsorption Data at 77 K," *J. Phys. Chem. B*, **106**, 4732–4739 (2002).

Lastoskie, C., K.E Gubbins,. and N. Quirke, "Pore Size Distribution Analysis of Microporous Carbons: A Density Functional Theory Approach," *J. Phys. Chem.*, **97**, 4786–4796 (1993).

Madden, W.G., "Fluid Distributions in Random Media: Arbitrary Matrices," *J. Chem. Phys.*, **96**, 5422-5432 (1992).

Maddox, M.W., J.P. Olivier, and K.E. Gubbins, "Characterization of MCM-41 Using Molecular Simulation: Heterogeneity Effects," *Langmuir*, **13**, 1737–1745 (1997).

Morishige, K. and M. Ito, "Capillary Condensation of Nitrogen in MCM-41 and SBA-15," *J. Chem. Phys.*, **117**, 8036–8041 (2002).

Morishige, K. and Y. Nakamura, "Nature of Adsorption and Desorption Branches in Cylindrical Pores," *Langmuir*, **20**, 4503–4506 (2004).

Neimark, A.V., P.I. Ravikovitch, M. Grün, F. Schüth, and K.K. Unger, "Pore Size Analysis of MCM-41 Type Adsorbents By Means of Nitrogen and Argon Adsorption," *J. Colloid Interface Science*, **207**, 159–169 (1998).

Neimark, A.V., P.I. Ravikovitch, and A. Vishnyakov, "Adsorption Hysteresis in Nanopores," *Phys. Rev. E*, **62**, 1493–1496 (2000).

Neimark, A.V. and P.I. Ravikovitch, "Capillary Condensation in MMS and Pore Structure Characterization," *Microporous and Mesoporous Materials*, **44–45**, 697–707 (2001).

Papadopoulou, A., F. van Swol, and U. Marini Bettolo Marconi, "Pore-End Effects on Adsorption Hysteresis in Cylindrical and Slitlike Pores," *J. Chem. Phys.*, **97**, 6942–6952 (1992).

Ravikovitch, P.I., D. Wei, W.T. Chueh, G.L. Haller, and A.V. Neimark, "Evaluation of Pore Structure Parameters of MCM-41 Catalyst Support and Catalysts by Means of Nitrogen and Argon Adsorption," *J. Phys. Chem. B.*, **101**, 3671–3679 (1997).

Ravikovitch, P.I. and A.V. Neimark, "Calculations of Pore Size Distributions in Nanoporous Materials from Adsorption and Desorption Isotherms," *Studies in Surf. Sci. & Catal.*, **129**, 597–606 (2000).

Ravikovitch, P.I., A. Vishnyakov, and A.V. Neimark, "Density Functional Theories and Molecular Simulations of Adsorption and Phase Transitions in Nanopores," *Phys. Rev. E*, **64**, 011602/1–011602/20 (2001).

Ravikovitch, P.I. and A.V. Neimark, "Characterization of Nanoporous Materials From Adsorption and Desorption Isotherms," *Colloids and Surfaces A: Physicochem. Eng. Aspects*, **187–188**, 11–21 (2001).

Rosenfeld, Y., "Free Energy Model for the Inhomogeneous Hard Sphere Fluid Mixture and Density Functional Theory of Freezing," *Phys. Rev. Lett.*, **63**, 980–983 (1989).

Schmidt, M., "Density-Functional Theory for Fluids in Porous Media," *Phys. Rev. E*, **66**, 041108/1–041108/7 (2002).

Selvam, P., S.K. Bhatia, and Ch. G. Sonwane, "Recent Advances in Processing and Characterization of Periodic Mesoporous MCM-41 Silicate Molecular Sieves," *Ind. Eng. Chem. Res.*, **40**, 3237–3261 (2001).

Sonwane, C.G. and S.K. Bhatia, "Adsorption in Mesopores: A Molecular-Continuum Model with Application to MCM–41," *Chem. Eng. Sci.*, **53**, 3143–3156 (1998).

Sonwane, C.G., S.K. Bhatia, and N. Calos, "Experimental and Theoretical Investigations of Adsorption Hysteresis and Criticality in MCM-41: Studies with O_2, Ar, and CO_2," *Ind. Eng. Chem. Res.*, **37**, 2271–2283 (1998).

Tarazona, P., "Free-Energy Density Functional for Hard Spheres," *Phys. Rev. A.*, **31**, 2672–2679 (1985).

Tarazona, P., U.M.B. Marconi, and R. Evans, "Phase Equilibria of Fluid Interfaces and Confined Fluids. Nonlocal Versus Local Density Functionals," *Mol. Phys.*, **60**, 573–595 (1987).

Thommes, M., R. Köhn, and M. Fröba, "Sorption and Pore Condensation Behavior of Pure Fluids in Mesoporous MCM-48 Silica, MCM-41 silica, SBA-15 Silica and Controlled-Pore Glass at Temperatures Above and Below the Bulk Triple Point," *Appl. Surf. Sci.*, **196**, 239–249 (2002).

Ustinov, E.A. and D.D. Do, "Application of Density Functional Theory to Capillary Phenomena in Cylindrical Mesopores with Radial and Longitudinal Density Distributions," *J. Chem. Phys.*, **120**, 9769–9781 (2004a).

Ustinov, E.A. and D.D. Do, "Capillary Phenomena in the Framework of the Two-Dimensional Density Functional Theory." *Fundamentals of Adsorption 8.* Sedona, Arizona, USA. May 23–28 2004b.

Ustinov, E.A., D.D. Do, and M. Jaroniec, "Application of Density Functional Theory to Equilibrium Adsorption of Argon and Nitrogen on Amorphous Silica Surface," *Appl. Surf. Sci.*, **252**, 548–561 (2005a).

Ustinov, E.A., D.D. Do, and M. Jaroniec, "Adsorption of Argon and Nitrogen in Cylindrical Pores of MCM-41 Materials. Application of Density Functional Theory," *Appl. Surf. Sci.*, **252**, 1013–1028 (2005b).

Ustinov, E.A., D.D. Do, and M. Jaroniec, "Equilibrium Adsorption in Cylindrical Mesopores: A Modified Broekhoff and de Boer Theory Versus Density Functional Theory," *J. Phys. Chem. B*, **109**, 11653–11660 (2005c).

Vishnyakov, A. and A.V. Neimark, "Nucleation of Liquid Bridges and Bubbles in Nanoscale Capillaries," *J. Chem. Phys.*, **119**, 9755–9764 (2003).

White, J.A. and A. Gonzalez, "The Extended Variable Space Approach to Density Functional Theory in the Canonical Ensemble," *J. Phys. Condens. Mater.*, **14**, 11907–11919 (2002).

Weeks, J.D., D. Chandler, and H.C. Andersen, "Role of Repulsive Forces in Determining the Equilibrium Structure of Simple Liquids," *J. Chem. Phys.*, **54**, 5237–5247 (1971).